Journal of The Electrochemical Society, **158** (3) H249-H254 (2011)
0013-4651/2011/158(3)/H249/6/$28.00 © The Electrochemical Society

Investigation of the Structural and Optical Properties of Ge-doped SbTe Films with Various Sb:Te Ratios

Tae Dong Kang,[a] Andrei Sirenko,[a] Jun-Woo Park,[b] Hyun Seok Lee,[c] Suyoun Lee,[c] Jeung-hyun Jeong,[c] Byung-ki Cheong,[c] and Hosun Lee[b,z]

[a]*Department of Physics, New Jersey Institute of Technology, Newark, New Jersey 07102, USA*
[b]*Department of Applied Physics, Kyung Hee University, Yong-In 446-701, Korea*
[c]*Electronic Materials Center, Korea Institute of Science and Technology, Seoul 136-791, Korea*

In this study, we investigated the structural and optical properties of Ge-doped SbTe (Ge–ST) thin films with three differing compositions: $Ge_{0.06}Sb_{0.77}Te_{0.17}$ ($Ge–ST_H$), $Ge_{0.05}Sb_{0.70}Te_{0.25}$ ($Ge–ST_M$), and $Ge_{0.05}Sb_{0.64}Te_{0.31}$ ($Ge–ST_L$), grown on Si substrate by radio-frequency sputtering method. The films were annealed at 250°C for crystallization and their crystal structures were examined by X-ray diffraction. Compared to the X-ray diffraction spectra of the undoped SbTe, the Ge–ST thin films had a hexagonal structure with large stacking periods. Using Raman spectroscopy, we investigated the shift of the phonon mode frequencies (A_{1g} and E_g) of the films with varying Sb:Te ratios. We compared the dependence of the phonon frequencies of Ge–ST on the Sb content to those of the corresponding undoped SbTe. The composition dependence of the A_{1g} phonon frequency could be explained in terms of the linear extrapolation of Sb and Sb_2Te_3 crystals. By using spectroscopic ellipsometry, we measured the dielectric function of the thin films in the near-IR, visible, and ultraviolet spectral regions. The optical energy gaps and bandgaps of the amorphous and crystalline phases, respectively, were determined using linear extrapolation of the absorption coefficient. The optical gap energies of the amorphous Ge–ST films were determined to be about 0.5–0.6 eV, whereas the indirect bandgap energies of the crystalline films shrank substantially to about 0.15–0.2 eV.
© 2011 The Electrochemical Society. [DOI: 10.1149/1.3532547] All rights reserved.

Manuscript submitted April 21, 2010; revised manuscript received December 3, 2010. Published January 5, 2011.

Phase-change random access memory (PRAM), which utilizes fast and reversible phase changes between high resistivity amorphous and low resistivity crystalline phases of chalcogenides, has been commercialized and first-generation PRAM products are based on the use of $Ge_2Sb_2Te_5$ as the memory material. Other material systems including GeTe,[1] SnSe,[2] Ge_2Se_3/SnTe bilayer,[3] and Ge (or Ag/In)-doped SbTe [4] have been investigated in search of memory materials that can provide a higher set speed and a lower set resistance but with a reduced reset current as compared to $Ge_2Sb_2Te_5$. Among these material systems, Ge-doped SbTe (Ge–ST) has been identified as a good candidate for PRAM.[4-7] Ge–ST thin films have been utilized successfully in high speed phase-change optical recording applications.[8,9] Ge–ST belongs to the δ-phase field in the Sb–Te binary phase diagram near the eutectic composition of $Sb_{0.7}Te_{0.3}$. The characteristics of Ge–ST based on memory devices have been recently investigated.[4-6] For example, Jeong et al. investigated the set characteristics of PRAM cells with Ge–ST materials with two different Sb:Te ratios (4.53 and 2.08). For the material with a higher Sb:Te ratio (4.53), a set operation was completed within several tens of nanoseconds via nucleation-free crystallization, whereas the material with a lower Sb:Te ratio (2.08) rendered a slower set operation requiring several hundred nanoseconds for the nucleation-mediated crystallization.[5] Wu et al. compared Ge–ST with $Ge_2Sb_2Te_5$ for its potential use in phase-change memory with improved stability at various ambient temperatures, and found that the device characteristics such as the reset current, reset resistance, and set resistance of the Ge–ST devices varied significantly less with ambient temperature than the $Ge_2Sb_2Te_5$ devices.[6] Despite much interest in Ge–ST thin films for memory applications, their physical properties have not been investigated in detail. In particular, elementary information such as the dielectric functions and bandgap energies of Ge–ST thin films has rarely been reported. Recently, Prokhorov et al. studied the effect of Ge addition on the optical and electrical properties of $Sb_{0.7}Te_{0.3}$ films by using optical transmission, reflectance, ellipsometry, and resistance measurements.[7]

In this work, we examined the structural and optical properties of Ge–ST thin films with three different Sb:Te ratios. We examined the phase states of the as-deposited and annealed films by X-ray diffraction, investigated the phonon modes by using Raman spectroscopy, and measured the dielectric functions from the near-IR to ultraviolet spectral ranges by using spectroscopic ellipsometry. From the estimated dielectric function, we determined the indirect bandgap (optical transition) energies of the crystalline (amorphous) films. We found that the transition energy decreased substantially from 0.5–0.6 to 0.15–0.2 eV after crystallization.

[z] E-mail: hlee@khu.ac.kr

Experimental

We grew Ge–ST thin films on Si substrates by using a radio-frequency sputtering method. We used Ge–ST targets with three different Sb:Te ratios belonging to the δ-phase field of the Sb–Te binary phase diagram.[10] The nominal thickness of the Ge–ST films was 100 nm. The compositions of the films were $Ge_{0.06}Sb_{0.77}Te_{0.17}$ ($Ge–ST_H$), $Ge_{0.05}Sb_{0.70}Te_{0.25}$ ($Ge–ST_M$), and $Ge_{0.05}Sb_{0.64}Te_{0.31}$ ($Ge–ST_L$) as measured by X-ray fluorescence spectrometry. The films were annealed at 250°C in an Ar gas environment for 30 min. The crystallinity of the annealed thin films was examined by obtaining θ-2θ scans in a BEDE D8 Discover X-ray diffractometer. The Raman measurements were performed at room temperature by using a Raman setup equipped with a single-grating 500 M spectrometer and a charge-coupled device detector. An Ar^+ laser with a wavelength of 514.5 nm was used for excitation at a power of 0.1 mW/μm^2. The laser power was set at the lowest possible value to prevent laser-induced annealing.

We measured the ellipsometric angles (Ψ,Δ) of the Ge–ST thin films by using spectroscopic ellipsometry (VASE model, J.A. Woollam Inc.) at room temperature at incidence angles of 65, 70, and 75°. In order to improve the accuracy of the dielectric function, we employed an autoretarder.

Results and Discussion

X-ray diffraction measurement.— Figure 1 shows the X-ray diffraction curves of the Ge–ST compounds: (a) $Ge–ST_H$, (b) $Ge–ST_M$, and (c) $Ge–ST_L$, plotted as a function of the inverse of the interplane distance d, which is equivalent to the scattering q-vector divided by 2π. The interplane distance d is related to the angle of diffraction θ by the Bragg equation $2d \sin \theta = n\lambda$. Our peak analysis showed that all measured crystalline thin films have hexagonal structures. Specifically, the peak positions of the crystalline Ge–ST films agree well with those of the long-period-stacking structures for undoped binary Sb–Te materials with a δ-phase.[11] For comparison, some of the major peak positions from Ref. 11 for three different Sb:Te contents

Downloaded 24 Mar 2011 to 130.199.3.165. Redistribution subject to ECS license or copyright; see http://www.ecsdl.org/terms_use.jsp

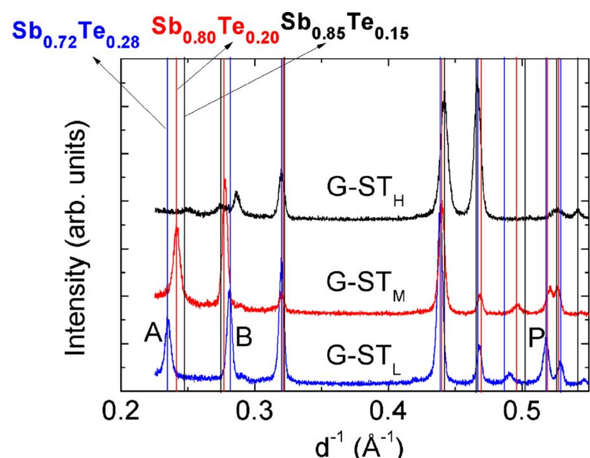

Figure 1. (Color online) X-ray diffraction curves of Ge-doped SbTe: Ge–ST_H($Ge_{0.06}Sb_{0.77}Te_{0.17}$), Ge–$ST_M$($Ge_{0.05}Sb_{0.70}Te_{0.25}$), and Ge–$ST_L$($Ge_{0.05}Sb_{0.64}Te_{0.31}$), plotted as a function of the inverse of the inter-plane distance d. For comparison, the vertical lines designating the major peak positions of Sb_xTe_{1-x} (x = 0.85, 0.80, 0.72) alloys obtained from Ref. 11 are also plotted.

(Sb:Te of 85:15, 80:20, and 72:28) are denoted as three different lines in Fig. 1. Note that Ge atoms substitute Sb atoms in the Ge–ST thin films. The Ge–ST thin films had similar compositions of (Ge + Sb):Te = 83:17, 75:25, and 69:31. In the case of the δ-phase SbTe compounds, they have A7 crystal structures as a basic crystal structure with additional large-period modulation such that the Sb layers comprising Sb–Sb bonds are stacked with Sb_2Te_3 layers. The number of Sb layers increases with increasing Sb content, leading to an increase in the unit cell size along the c-direction.[11-13] The symbols A, B, and P are attached to the diffraction peaks in Fig. 1. Based on the X-ray and transmission electron diffraction study of Ref. 11, P is a diffraction peak corresponding to the spacing of a fundamental lattice plane perpendicular to the c-axis, and A and B are diffraction peaks reflecting the long period structure along the c-axis. Denoting the origin $d^{-1} = 0$ as O in Fig. 1, M (= OP/AB) corresponds to a stacking period of the superlattice because AB and OP correspond to the length of superlattice unit cell and the mean spacing of one atomic layer in the hexagonal structure, respectively. The stacking periods of Ge–ST_L, Ge–ST_M, and Ge–ST_H were 11.3 ± 0.2, 14.5 ± 0.2, and 21.0 ± 0.5, respectively. For comparison, the equivalent Sb–Te binary compounds were estimated to have respective stacking periods of 9.8, 12.1, and 17.7 for the same Te contents, according to Kifune et al.[11] Despite the similar trend of change as a function of the Sb to Te content, the stacking periods of the Ge–ST films are not identical to those of the equivalent undoped Sb–Te but are larger by 1.5, 2.4, and 3.3 layers, respectively. These differences may be accounted for by errors of several atom percent in the measured compositions of Ge–ST films, which appears to be an unreasonable explanation. Therefore, we consider that the increased stacking periods of the Ge–ST materials may be due to the effects of the Ge addition. This is because bonding configurations, particularly in the Sb_2Te_3 layers of the long-period structures, would be perturbed by the added Ge atoms that would obviously prefer different coordinations with Te atoms. It is also noted that the large stacking layers in the unit cells of Ge–ST in this work are in contrast to the work reported by Matsunaga and Yamada.[14] They reported that laser-crystallized Ge–ST and (Ag, In)-doped SbTe materials have the A7 crystal structure of Sb crystals at room temperature without the long-period modulation, although undoped SbTe has a superlattice structure with a large number of stacking periods.[11,14] These differing results of the two different studies may be ascribed to the slight difference of Ge content (by about 1.5 atom%) and possibly the differences in the thin-film growth conditions as well.

Raman spectra.— Figure 2 shows the Raman spectra of the (a) amorphous and (b) crystalline phases of Ge–ST: Ge–ST_H, Ge–ST_M, and Ge–ST_L. The Raman spectra for all of the measured amorphous Ge–ST films (Fig. 2a) look almost the same regardless of the Sb:Te

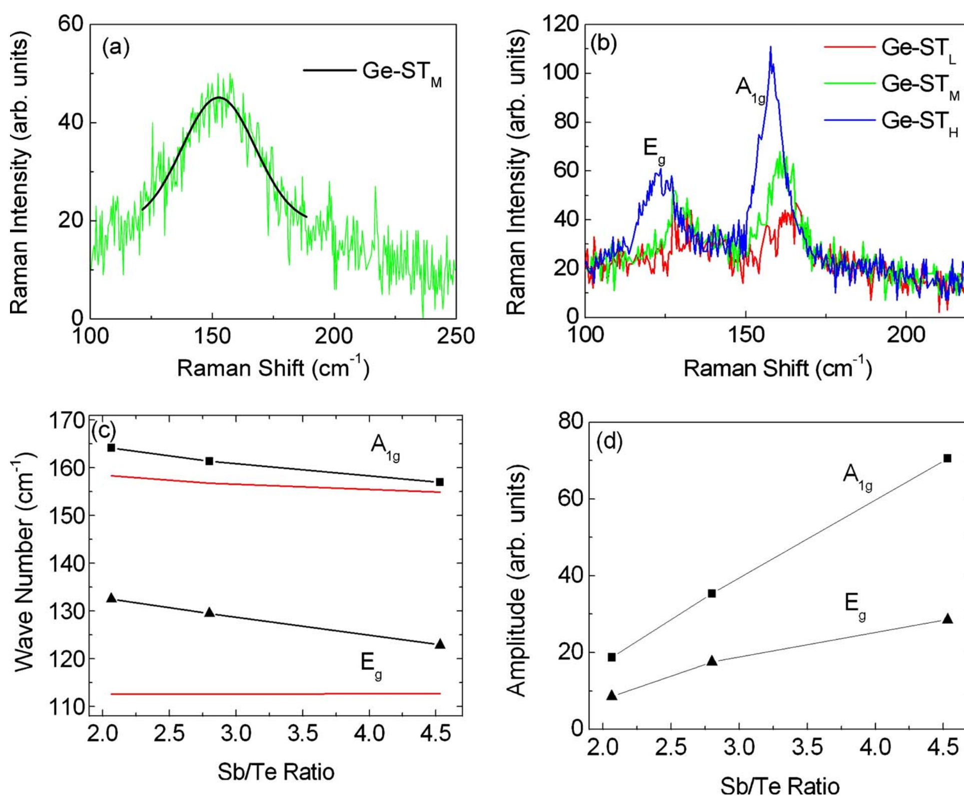

Figure 2. (Color online) Raman intensity of (a) as-deposited and (b) annealed Ge–ST films with different Sb:Te ratios for Ge-doped SbTe compounds. The best-match Gaussian curve is also plotted in (a). The measured frequencies and amplitudes of two Raman modes are plotted in (c) and (d), respectively, as a function of the Sb:Te ratio. The red lines are linearly interpolated values of the phonon modes of undoped SbTe compounds between those of the end point materials, Sb and Sb_2Te_3. The error bars of the phonon frequencies of the amorphous and the crystalline phases were obtained with Gaussian curve fitting and were about 0.5 and 0.3 cm^{-1}, respectively.

Downloaded 24 Mar 2011 to 130.199.3.165. Redistribution subject to ECS license or copyright; see http://www.ecsdl.org/terms_use.jsp

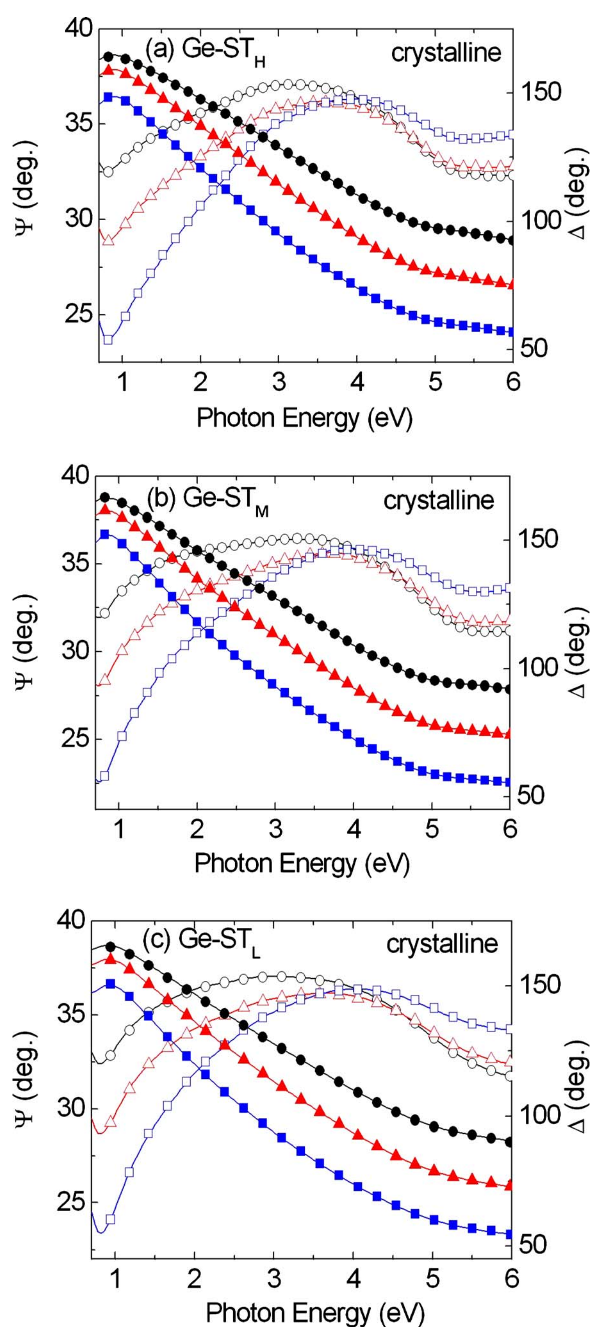

Figure 3. (Color online) The raw and the best-match ellipsometry angles (Ψ,Δ) for the crystalline thin films of (a) Ge–ST$_H$, (b) Ge–ST$_M$, and (c) Ge–ST$_L$. The filled and unfilled discrete symbols designate the raw data of Ψ and Δ, and the lines denote their best-match curves. Here, circles, triangles, and rectangles represent angles of incidence of 65, 70, and 75°, respectively.

ratio with a single broad peak centered at around 152 cm^{-1} with a full width at half-maximum (fwhm) of 50 cm^{-1}. The phonon peak was fitted by using a Gaussian line shape. The phonon peak frequency did not change within the error bar of 0.6 cm^{-1}. The broad Raman peak of the amorphous Ge–ST films can be ascribed mainly to the Sb components.[15-17] As shown in Fig. 2b, two Raman modes of the crystalline Ge–ST films appear at around 125 and 160 cm^{-1}, identified as E_g and A_{1g} modes, respectively.[17,18] Rossow et al. showed that the Raman characteristic of amorphous Sb films, i.e., a broad spectrum between 120 and 170 cm^{-1}, changed to E_g and A_{1g} phonon lines of crystalline Sb due to the amorphous-to-polycrystalline phase transition, settling in at the certain thickness of the Sb film layer.[17,19] According to the literature, both Sb and Sb_2Te_3 have a hexagonal structure and the phonon frequencies of E_g (Sb), A_{1g} (Sb), E_g (Sb_2Te_3), and A_{1g} (Sb_2Te_3) are 113, 151, 112, and 165 cm^{-1}, respectively.[17,18,20]

Table I. The estimated surface roughness and the main layer thicknesses of the Ge–ST thin films.

		Surface roughness (nm)	Main layer (nm)	Total layer thickness (nm)
Ge–ST$_H$	Amorphous	3.7	94.8	98.5
	Annealed	11.8	79.8	91.6
Ge–ST$_M$	Amorphous	3.0	103.5	106.5
	Annealed	6.7	91.4	98.1
Ge–ST$_L$	Amorphous	3.9	91.1	95.0
	Annealed	4.3	84.1	88.4

In Ge-doped SbTe compounds, $Ge_ySb_xTe_{1-x-y}$ ($y \ll x$), the phonon frequencies are expected to be roughly the same as those of undoped SbTe, $Sb_{x+y}Te_{1-x-y}$. Therefore, the phonon frequencies of $Ge_{0.05}Sb_xTe_{0.95-x}$ were compared to those of $Sb_{x+0.05}Te_{0.95-x}$, which were interpolated from literature values of Sb and Sb_2Te_3 in Fig. 2c.[17,18] Figures 2c and 2d show the frequencies and amplitudes of the E_g and A_{1g} modes as a function of Sb:Te composition ratio, respectively. The frequencies of both the E_g and A_{1g} modes decreased with the increase of the Sb composition, while the amplitudes of the two peaks increased. The decrease of the A_{1g} frequencies with increasing Sb composition is consistent with the linear interpolation of the phonon frequencies of Sb and Sb_2Te_3. For the A_{1g} mode, the decrease of the frequencies and the increase of the amplitudes are linearly proportional to the Sb/Te composition ratio or to the stacking period ($M = 2n + 3$ for $Sb_{2n}Te_3$) of the crystal structures of the corresponding binary Sb–Te materials.[11] Experimentally the magnitudes of the frequency shifts of the E_g and A_{1g} modes are very similar to each other.

In Fig. 2c, the Ge doping affects the E_g frequencies significantly because the phonon frequencies are larger by about 15 cm^{-1} than the interpolated frequencies of Sb and Sb_2Te_3. We consider that this is because Ge atoms are much lighter than Sb and Te atoms. The E_g mode frequencies of bulk Sb and Sb_2Te_3, the end point materials, are roughly the same as each other.[5] However, we note that the measured frequencies of the E_g modes decreased with increasing Sb content. According to Ref. 5, the grain size increases substantially as the Sb composition increases. The grain size distributions of the Ge–ST alloys were obtained from the transmission electron microscopy data where the grain sizes of Ge–ST$_L$, Ge–ST$_M$, and Ge–ST$_H$ increased dramatically with increasing Sb composition with average grain sizes of about 100 nm, 500 nm, and 5 μm, respectively.[5] Considering the dramatic increase of the grain size in the Ge–ST films with the increase of the Sb content, the increase of the amplitudes of E_g and A_{1g} of the Ge–ST films may be due to the grain size effect. With increasing grain size, the crystallinity should increase and the amplitude of the crystalline phonon should increase.

Spectroscopic ellipsometry.— We estimated the dielectric functions and the thicknesses of the Ge–ST thin films by using multilayer model analysis and parametric optical constant (POC) model. We used a four-phase model that took into account surface roughness, the Ge–ST layer, SiO_2 layer (2 nm), and Si substrate. We employed the POC model developed by Johs et al.,[21] which can provide a Kramers-Kronig-consistent model dielectric function, and has been successfully applied to the dielectric functions of polymers as well as crystalline and amorphous semiconductors.[21,22] To model the surface roughness layer, we used the Bruggeman effective medium approximation with a mixture of the main layer (50%) and void (50%).[23]

The dielectric function of the main layer was fitted using the POC model, in which the dielectric function is written as the sum-

Downloaded 24 Mar 2011 to 130.199.3.165. Redistribution subject to ECS license or copyright; see http://www.ecsdl.org/terms_use.jsp

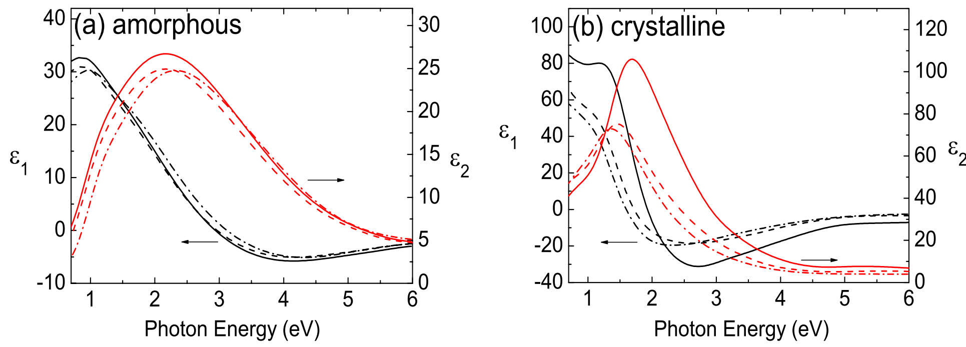

Figure 4. (Color online) The dielectric function spectra of (a) amorphous and (b) crystalline Ge–ST thin films of Ge–ST_H (solid line), Ge–ST_M (dashed line), and Ge–ST_L (dotted-dashed line). The black and red lines denote the real and the imaginary part of the dielectric functions ($\varepsilon = \varepsilon_1 + i\varepsilon_2$).

mation of "m" energy-bounded, Gaussian-broadened polynomials and P poles accounting for the index effects due to absorption outside the model region.[21] The POC model equation is Kramers-Kronig-consistent, and is given by

$$\varepsilon(E) = \varepsilon_1(E) + i\varepsilon_2(E) = 1 + i\sum_{j=1}^{m}\int_{E_{\min}}^{E_{\max}} W_j(E')\Phi(E,E',\sigma_j)dE' + \sum_{j=m+1}^{m+P+1}\frac{A_j}{E^2 - E_j^2} \quad [1]$$

where

$$\Phi(E,E',\sigma) = \int_0^\infty e^{i(E-E'+i2\sigma^2 s)s}ds - \int_0^\infty e^{i(E+E'+i2\sigma^2 s)s}ds = \sqrt{\frac{\pi}{8\sigma^2}}[e^{-y_1^2} + e^{-y_1^2}\operatorname{erf}(iy_1) - e^{-y_2^2} - e^{-y_2^2}\operatorname{erf}(iy_2)] \quad [2a]$$

$$y_1 = \frac{E - E'}{2\sqrt{2}\sigma} \qquad y_2 = \frac{E + E'}{2\sqrt{2}\sigma} \quad [2b]$$

and

$$W_j(E) = \sum_{k=0}^{N} P_{j,k}E^k u(E - a_j)u(b_j - E) \quad [3]$$

Here, $u(x)$ is the unit step function, and E_j, σ_j, and A_j are the energy threshold, broadening, and amplitude, respectively, for the jth optical gap structure. We used a modified POC model in WVASE32 software (provided by J. A. Woollam Inc.), which includes another fitting parameter E_{width}, which is used to connect two neighboring energy gaps.

Figure 3 shows the raw and the best-match ellipsometry angles (Ψ, Δ) for (a) Ge–ST_H, (b) Ge–ST_M, and (c) Ge–ST_L. The discrete symbols designate the raw data and the lines denote the best-match curves. Table I shows the estimated thicknesses of the thin films including the surface roughness and the main layer of Ge–ST. The error bars of the thicknesses are about 1 nm. For each film, the total

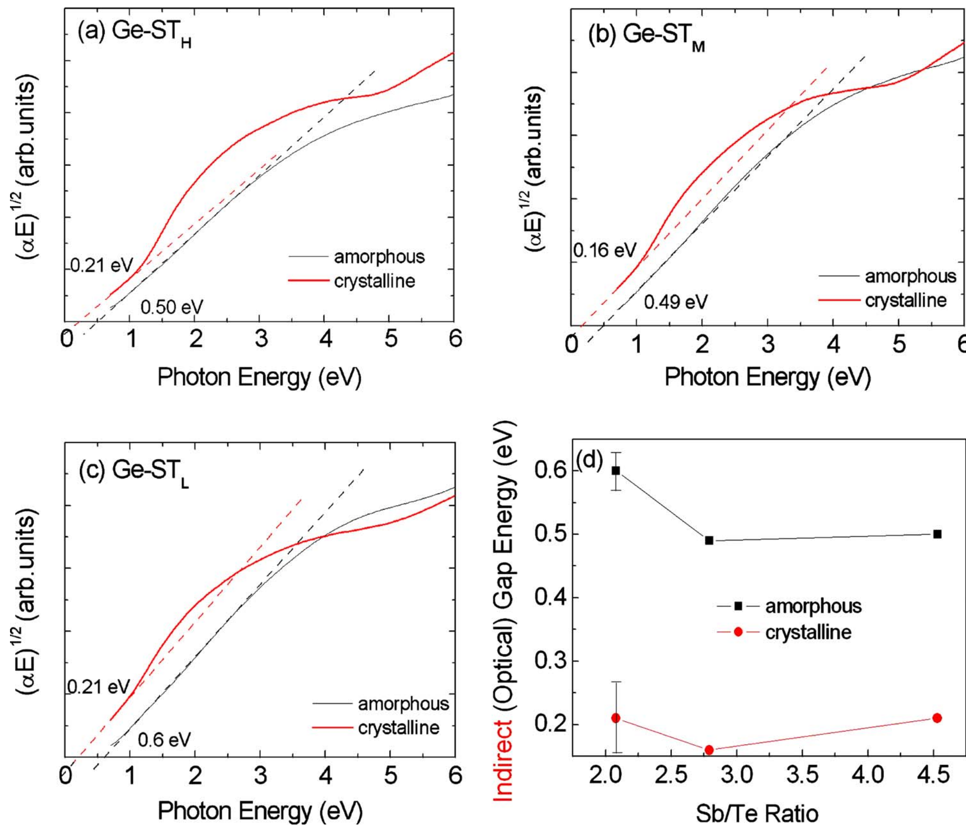

Figure 5. (Color online) The plot of $(\alpha E)^{1/2} = A(E - E_{\text{opt(ind)}})$ for (a) Ge–ST_H, (b) Ge–ST_M, and (c) Ge–ST_L to estimate the transition (bandgap) energies of the amorphous (crystalline) phase. (d) The plot of the corresponding optical (indirect) gap energies as a function of the Sb/Te ratio. The error bars are also designated in (d). The error bars are about 0.03 and 0.06 eV for the amorphous and crystalline phases of the Ge–ST alloys, respectively.

Downloaded 24 Mar 2011 to 130.199.3.165. Redistribution subject to ECS license or copyright; see http://www.ecsdl.org/terms_use.jsp

Table II. The estimated optical (indirect band)gap energy and optical transition (CP) energy of the amorphous (crystalline) phase.

	Amorphous Optical gap energy (eV)	Crystalline Indirect gap energy (eV)
Ge–ST_H	0.50	0.21
Ge–ST_M	0.49	0.16
Ge–ST_L	0.60	0.21

layer thickness decreased by about 7% due to the amorphous-to-crystalline phase transition. The surface roughness of the Ge–ST_L layer is about 4 nm and it changed very slightly after crystallization. However, for Ge–ST_M and Ge–ST_H, the surface roughness layer thickness increased by factors of 2 and 3, respectively, after annealing. Therefore, it is apparent that the crystalline thin films tend to have larger surface roughness values as the Sb content increases. This is consistent with our previous finding that the crystalline grain size increases remarkably from Ge–ST_L to Ge–ST_M, and to Ge–ST_H, as well as with our Raman results.[5] The finding was explained to be due to the rapidly increasing growth speed of crystallites with increasing Sb/Te ratio as well as the relatively faster nucleation kinetics for Ge–ST_L.[5]

Figure 4 shows the dielectric function spectra of the Ge–ST alloys. The dielectric functions of the amorphous Ge–ST thin films do not change significantly with increasing Sb composition. The amplitude of the dielectric functions increased substantially by a factor of 3 or 4 after crystallization. In particular, the dielectric function of the crystalline Ge–ST_H is the largest. The dominance of the dielectric function of Ge–ST_H may be partially related to its large grain size. The ε_2 spectrum of the annealed Ge–ST_H film in Fig. 4b shows that there is an optical structure below 1 eV. The large optical contrast between the amorphous and crystalline phases for $Ge_2Sb_2Te_5$ has been interpreted to be due to the resonance bonding model.[24] The same model may be applied for the Ge-doped SbTe thin films. The optical properties and electronic structural properties of (GeTe, Sb_2Te_3) pseudobinary thin films, e.g., GeTe, $Ge_2Sb_2Te_5$, $Ge_1Sb_2Te_4$, $Ge_1Sb_4Te_7$, and Sb_2Te_3, with increasing Sb/Ge atomic ratio were reported for amorphous and stable phases by Park et al.[25,26] According to Shportko et al.,[24] the dielectric functions of (GeTe, Sb_2Te_3) pseudobinaries in the IR and visible energy ranges reveal that the optical dielectric constant (ε_∞) is 70–200% larger for the crystalline phase than the amorphous phases. This difference is attributed to a significant change in bonding between the two phases involving the covalent bonding of the amorphous phase and the resonant bonding of the crystalline phase. The large optical contrast between the amorphous and crystalline phases is used for applications in high speed optical recording.

Figure 5 shows the plot of $(\alpha E)^{1/2} = A(E - E_{opt(ind)})$ for the Ge–ST thin films used to determine the optical gap energy E_{opt} (indirect bandgap energy E_{ind}) by using a linear extrapolation method where $\alpha(= 4\pi k/\lambda)$ is the absorption coefficient and E is the photon energy.[27] The complex refractive index ($N = n + ik$) is the square root of the dielectric function ($\varepsilon = \varepsilon_1 + i\varepsilon_2$). For example, in Fig. 5a the linearly extrapolated lines for amorphous and crystalline Ge–ST_H thin films cross the energy axis at 0.50 and 0.21 eV, respectively. We note that the error bar of the indirect gap energy for the Ge–ST alloys is large due to the narrow linear region of $(\alpha E)^{1/2}$. The optical (band)gap energy is given by $(\alpha E)^n = C(E - E_g)$, where $n = 1/2$ for the optical (band)gap of amorphous (indirect gap and crystalline) semiconductors and $n = 2$ for direct gap semiconductors with a crystalline phase. For $n = 2$, we did not observe a linear region below 2 eV for the crystallized Ge–ST, whereas $n = 1/2$ provided optical (band)gap energies below or near 0.5 eV.[27] Table II summarizes the estimated optical (indirect band)gap energy of the amorphous (crystalline) thin films. In the case of Ge–ST_M, the optical energy gaps of the amorphous and crystalline phases are 0.49 and 0.16 eV, respectively. Reference 7 reported a similar value of 0.47 eV for the amorphous phase of the same composition. The optical gap energy of the amorphous Ge–ST alloys decreases with increasing Sb content as expected, as the increasing Sb content should decrease the bandgap energy. Including the error bar, we did not find any composition dependence of the indirect bandgap energy of the crystalline phase for the Ge–ST alloys. The optical gap (indirect bandgap) energy of the amorphous (crystalline) $Ge_2Sb_2Te_5$ has been reported by several groups. For example, Park et al. reported optical transition and indirect bandgap energies of 0.8 and 0.57 eV, respectively, for $Ge_2Sb_2Te_5$.[26] For comparison, the bandgap energies of the Ge–ST thin films are much smaller than that of $Ge_2Sb_2Te_5$ because of the larger Sb content.

Conclusion

We measured the ellipsometric angles (Ψ and Δ) of Ge–ST thin films deposited on Si substrate with different compositions of $Ge_{0.06}Sb_{0.77}Te_{0.17}$(Ge–$ST_H$), $Ge_{0.05}Sb_{0.70}Te_{0.25}$(Ge–$ST_M$) and $Ge_{0.05}Sb_{0.64}Te_{0.31}$(Ge–$ST_L$). The films were annealed at 250°C and were found to have a hexagonal structure. From the X-ray diffraction spectra, we found that Ge–ST thin films had a superlattice structure with large stacking periods. The stacking periods (M) of Ge–ST were comparable to those of undoped SbTe with the same Te contents. We examined the Raman spectroscopic characteristics of the Ge–ST films and observed that the crystalline films display the phonon modes of E_g and A_{1g}, where the wave numbers and amplitudes changed with increasing Sb content. The Sb composition dependence of the phonon frequencies of the Ge–ST films were explained in terms of the linear extrapolation between Sb and Sb_2Te_3 crystals. By using the POC model and multilayer model analysis, we estimated the dielectric functions of the Ge–ST thin films. We determined the optical energy gaps and the indirect bandgaps for amorphous and crystalline phases, respectively, by linear extrapolation of the absorption coefficient. The optical gap energies of the amorphous phases of Ge–ST were estimated to be 0.5–0.6 eV, whereas the indirect bandgap energies of the crystalline phases were much smaller at 0.15–0.2 eV. These values are smaller than those of $Ge_2Sb_2Te_5$ by 0.2–0.3 and 0.4 eV for the amorphous and crystalline phases, respectively, due to the increase of the Sb content. This work verified the electronic and vibrational properties as well as the structural properties of the Ge–ST thin films.

Acknowledgments

The work at Kyung Hee University was supported by the National Research Foundation grant no. 2010-0015824, and the work at KIST was supported by the National Research Program for 0.1 Terabit Nonvolatile Memory Devices sponsored by the Korean Ministry of Knowledge Economy.

National Research Foundation assisted in meeting the publication costs of this article.

References

1. S. Raoux, B. Muñoz, H.-Y. Cheng, and J. L. Jordan-Sweet, *Appl. Phys. Lett.*, **95**, 143118 (2009).
2. K.-M. Chung, D. Wamwangi, M. Woda, M. Wuttig, and W. Bensch, *J. Appl. Phys.*, **103**, 083523 (2008).
3. A. Devasia, F. Bai, M. Davis, K. A. Campbell, S. Gupta, and S. Kurinec, *Thin Solid Films*, **517**, 6516 (2009).
4. M. H. R. Lankhorst, B. W. S. M. M. Ketelaars, and R. A. M. Wolters, *Nature Mater.*, **4**, 347 (2005).
5. J.-h. Jeong, H. S. Lee, S. Lee, T. S. Lee, W. M. Kim, W. Zhe, S. C. Kim, K. H. Oh, and B. Cheong, *J. Phys. D: Appl. Phys.*, **42**, 035104 (2009).
6. Z. Wu, S. Lee, Y.-W. Park, H.-W. Ahn, D. S. Jeong, J.-h. Jeong, K. No, and B.-k. Cheong, *Appl. Phys. Lett.*, **96**, 133510 (2010).
7. E. Prokhorov, A. Mendoza-Galván, J. González-Hernández, and B. Chao, *J. Non-Cryst. Solids*, **353**, 1870 (2007).
8. M. Hone, N. Nobukuni, K. Kiyono, and T. Ohno, *Proc. SPIE*, **4090**, 135 (2000).
9. N. Nakamura, N. Morishita, K. Suzuki, K. Yusu, K. Ichihara, M. Kuwahara, H. Hasekawa, and H. Kobori, *Jpn. J. Appl. Phys., Part 1*, **37**, 3339 (1998).
10. S. Bordas and M. T. Clavaguera-Mora, *Thermochim. Acta*, **107**, 239 (1986).
11. K. Kifune, Y. Kuita, T. Matsunaga, and N. Yamada, *Acta Crystallogr., Sect. B:*

Downloaded 24 Mar 2011 to 130.199.3.165. Redistribution subject to ECS license or copyright; see http://www.ecsdl.org/terms_use.jsp

Struct. Sci., **B61**, 492 (2005).
12. C. W. Sun, J. Y. Lee, M. S. Youm, and Y. T. Kim, *Jpn. J. Appl. Phys., Part 1*, **45**, 9157 (2006).
13. JCPDS Inorganic no. 46–1068, International Center for Diffraction Data, Newton Square, PA (2003).
14. T. Matsunaga and N. Yamada, *Jpn. J. Appl. Phys., Part 1*, **43**, 4704 (2004).
15. J. S. Lannin, *Phys. Rev. B*, **15**, 3863 (1977).
16. K. S. Andrikopoulos, S. N. Yannopoulos, A. V. Kolobov, P. Fons, and J. Tominaga, *J. Phys. Chem. Solids*, **68**, 1074 (2007).
17. U. Rossow, U. Frotscher, N. Esser, U. Resch, Th. Müller, W. Richter, D. A. Woolf, and R. H. Williams, *Appl. Surf. Sci.*, **63**, 35 (1993).
18. W. Richter, H. Köhler, and C. R. Becker, *Phys. Status Solidi B*, **84**, 619 (1977).
19. M. Hünermann, J. Geurts, and W. Richter, *Phys. Rev. Lett.*, **66**, 640 (1991).
20. G. C. Sosso, S. Caravati, and M. Bernasconi, *J. Phys.: Condens. Matter*, **21**, 095410 (2009).
21. B. Johs, C. M. Herzinger, J. H. Dinan, A. Cornfeld, and J. D. Benson, *Thin Solid Films*, **313–314**, 137 (1998).
22. R. Schmidt-Grund, A. Carstens, B. Rheinländer, D. Spemann, H. Hochmut, G. Zimmermann, M. Lorenz, M. Grundman, C. M. Herzinger, and M. Schubert, *J. Appl. Phys.*, **99**, 123701 (2006).
23. D. E. Aspnes, *Thin Solid Films*, **89**, 249 (1982).
24. K. Shportko, S. Kremers, M. Woda, D. Lencer, J. Robertson, and M. Wuttig, *Nature Mater.*, **7**, 653 (2008).
25. J.-W. Park, S. H. Baek, T. D. Kang, H. Lee, Y.-S. Kang, T.-Y. Lee, D.-S. Suk, K. J. Kim, C. K. Kim, Y. H. Khang, et al., *Appl. Phys. Lett.*, **93**, 021914 (2008).
26. J.-W. Park, S. H. Eom, H. Lee, J. L. F. Da Silva, Y.-S. Kang, T.-Y. Lee, and Y. H. Khang, *Phys. Rev. B*, **80**, 115209 (2009).
27. B. S. Lee, J. R. Abelson, S. G. Bishop, D. H. Kang, B. K. Cheong, and K. B. Kim, *J. Appl. Phys.*, **97**, 093509 (2005).

Downloaded 24 Mar 2011 to 130.199.3.165. Redistribution subject to ECS license or copyright; see http://www.ecsdl.org/terms_use.jsp